

CONTINUOUS-TIME STATE-SPACE UNSTEADY AERODYNAMIC MODELLING FOR EFFICIENT AEROELASTIC LOAD ANALYSIS

Noud P.M. Werter¹, Roeland De Breuker², Mostafa M. Abdalla²

¹ Delft University of Technology
Kluyverweg 1, 2629 HS, Delft, the Netherlands
n.p.m.werter@tudelft.nl

² Delft University of Technology
Kluyverweg 1, 2629 HS, Delft, the Netherlands

Keywords: unsteady aerodynamics, state-space, loads.

Abstract: Over the years, wings have become lighter and more flexible, making them more prone to aeroelastic effects. Thus, aeroelasticity in design becomes more important. In order to determine the response of an aircraft to, for example, a gust, an unsteady aerodynamic model is required to determine the dynamic loads. The three most-commonly used methods in aeroelastic loads analysis are 2D unsteady-airfoil theory, the doublet lattice method (DLM), and the unsteady vortex lattice method (UVLM). In contrast to these existing methods, the current paper proposes a 3D state-space model for unsteady aerodynamic analysis that is both directly written in time-domain, and is a continuous-time model. The main advantages of this are that no approximation errors are made in the conversion to the time domain, and that the time step is only driven by requirements on accuracy. The model is based on potential flow theory, which is implemented by means of vortex ring elements. The model was first verified, and then applied to a pitch-plunge response problem showing the benefits of the current approach over existing methods.

1 INTRODUCTION

One of the driving parameters in the design of aircraft has always been reducing weight to reduce the operating cost and make them more efficient. As a consequence, wings have become more flexible, making aeroelasticity more important in aircraft wing design. In order to determine the dynamic response of an aircraft to, for example, a gust, an unsteady aerodynamic model is required to determine the dynamic loads.

There are several ways to predict the unsteady aerodynamic loads on an aircraft. Murua et al.[1] and Kier[2] give a nice overview of unsteady aerodynamic modelling for loads analysis. The three most-commonly used methods are 2D unsteady-airfoil theory, the doublet lattice method (DLM), and the unsteady vortex lattice method (UVLM). A brief overview of each of these methods will be given in the following paragraphs.

2D unsteady-airfoil theory is generally referred to as strip theory. It uses closed-form solutions for several specific cases (i.e. impulsive flows, step gusts, harmonic oscillations, and sinusoidal gusts) in order to set up a state-space system to determine the unsteady aerodynamic loads. Strip theory has extensively been used for high-altitude-long-endurance (HALE) aircraft modelling [3, 4]. Two different methods to obtain a state-space system from the closed-form solutions are commonly used: Peters' finite-state method[5] and the indicial

method of Leishman[6]. The main advantages of strip theory are its simplicity and that it allows for easy corrections for, for example, stall. However, the main disadvantage of strip theory is that it is based on 2D unsteady-airfoil theory with 3D corrections and thus it cannot give any accurate information about the spanwise loading distribution. The doublet lattice method, introduced by Albano and Rodden[7], is probably the most-widely used method for unsteady load analysis of aircraft. DLM assumes harmonic displacements on the natural vibration modes of the wing to determine the aerodynamic influence coefficients (AICs) for several reduced frequencies and flight conditions. The solution is converted from the frequency domain to the time domain by means of a rational function approximation (RFA). There are two well-known techniques for the RFA: Roger's approach using Padé approximants[8] and Karpel's minimum-state method[9]. The setup in the frequency domain makes the method especially suitable for flutter analysis. However, when time domain simulations are required, an incorrect selection of lag terms in the RFA can have a significant effect on the accuracy of the results. Furthermore, a wide range of reduced frequencies has to be covered to ensure accurate results.

The unsteady vortex lattice method uses a distribution of vortex rings over the mean aerodynamic surface to solve the potential flow equations. Katz and Plotkin[10] give a good overview of the implementation of UVLM. The main advantage of UVLM is that it allows for modelling a free wake and can thus be used for the computation of the flow around wings undergoing large motions. Therefore UVLM has recently become popular for the accurate analysis of HALE aircraft wings undergoing large deformations[1]. Furthermore, UVLM can be written in a discrete-time state-space system[11], allowing easy integration with other disciplines. However, this also immediately highlights the main disadvantage of UVLM: the solution can only be obtained using a fixed time step. This can result in inefficient analysis when, for example, the structural model or the flight dynamic model would allow for larger time steps to be used.

As can be concluded from the previous paragraphs, all three methods have their own advantages and disadvantages. Ideally one would want a 3D unsteady aerodynamic analysis model, which is directly written in time-domain and is a continuous-time model, such that no approximation errors are made in the conversion to the time domain and the most efficient time step can be used for the analysis. Therefore the current paper proposes a 3D continuous-time state-space model for unsteady aerodynamic analysis. This work is based on the work of Mohammadi-Amin et al.[12] This paper extends their model to the application of arbitrary wing planforms, camber distribution, and twist distribution and instead of constant strength doublet panels, vortex ring elements are used to simplify the computation of aerodynamic forces on non-uniform meshes. Section 2 will give a brief overview of the potential flow theory on which the aerodynamic model is based, followed by the implementation of this potential flow theory in a continuous-time state-space model by means of vortex rings. Section 3 will then show the verification of this model and its application to determining the gust response of an aircraft. Finally conclusions will be drawn on the application of the model for efficient aeroelastic analysis.

2 UNSTEADY AERODYNAMIC MODEL

For efficient loads analysis, the unsteady aerodynamic model is based on potential flow theory. When the flow conditions around a wing correspond to low to moderate subsonic Mach numbers, very high Reynolds numbers, and small angles of attack, the incompressible,

inviscid, and irrotational flow assumptions are valid. In this case, the Navier-Stokes equations can be reduced to the Laplace equation for the velocity potential, ϕ :

$$\nabla^2 \phi = 0 \quad (1)$$

In order to solve this problem, the solution is subject to a set of boundary conditions. In aerodynamics of aircraft, these in general consist of a boundary condition enforcing flow tangency on the wing surface and a boundary condition at infinity that ensures the flow disturbance vanishes at infinity:

$$(\nabla \phi + \mathbf{V}_\infty) \cdot \mathbf{n} = 0, \text{ on the wing surface} \quad (2)$$

$$\lim_{|\mathbf{x} - \mathbf{x}_0| \rightarrow \infty} \nabla \phi = 0 \quad (3)$$

where \mathbf{V}_∞ is the free-stream velocity vector, \mathbf{n} is the surface normal vector, \mathbf{x}_0 is the position vector on the wing surface, and \mathbf{x} is the position vector of the location of interest.

Once the potential difference over the wing surface is determined, the aerodynamic pressures can be computed using the unsteady Bernoulli equation:

$$\frac{p_\infty - p}{\rho} = \frac{1}{2} (\nabla \phi)^2 + \frac{\partial \phi}{\partial t} \quad (4)$$

Given these pressures, the unsteady aerodynamic forces and moments can be computed using the panel geometry.

In aerodynamics, the potential flow solution is commonly obtained using the boundary element method. The first step in the solution of the aerodynamic flow around the wing by means of the boundary element method is the selection of the type of singularity element, i.e. elementary solutions to the Laplace equation. All singularity elements commonly used in aerodynamics, e.g. sources, doublets, or vortices, automatically satisfy the far-field boundary conditions. In this case, vortex ring elements have been selected, since they allow for simple meshing of any arbitrary thin wing surface and the corresponding aerodynamic forces can be computed directly from their strength by using the Kutta-Joukowski theorem. Katz and Plotkin[10] provide a detailed description of the solution of the unsteady flow around a wing by means of vortex ring elements, resulting in the equation for the flow tangency boundary condition. In contrast to Katz and Plotkin where this equation is solved using a time-stepping procedure and the wake is developed in time, similar to Mohammadi-Amin et al.[12] for constant strength doublet panels, under the assumption of small motions about a reference configuration, a prescribed wake can be included and using the Kutta condition and Helmholtz theorem, a complete system of equations for vortex ring elements can be found and is given by:

$$\mathbf{A} \boldsymbol{\Gamma}^t = -\mathbf{V}_\infty \cdot \mathbf{n}, \text{ Flow tangency condition} \quad (5)$$

$$\boldsymbol{\Gamma}_{TE}^t = \boldsymbol{\Gamma}_{w_0}^t, \text{ Kutta condition} \quad (6)$$

$$\mathbf{H}_1 \boldsymbol{\Gamma}^t = \mathbf{H}_2 \boldsymbol{\Gamma}^{t-1}, \text{ Helmholtz theorem} \quad (7)$$

where \mathbf{A} is the matrix of aerodynamic influence coefficients, $\boldsymbol{\Gamma}^t$ is the vector of unknown vortex ring strengths at time t , $\boldsymbol{\Gamma}_{TE}$ is the vector of unknown vortex ring strengths at the

trailing edge of the wing, Γ_{w_0} is the vector of unknown vortex ring strengths at the start of the wake, and matrices \mathbf{H}_1 and \mathbf{H}_2 describe the transport of vorticity in the wake. An example of a corresponding wing discretization is shown in Figure 1, illustrating the different vortex rings. Note that, as can be seen, the first wake panel is smaller than any following wake panels. From a physical point of view, this can be interpreted by looking at the starting vortex. At the first time step, when the vortex strength in the wake is still 0, the closing vortex of the first wake panel can be interpreted as the starting vortex that develops following the trailing edge angle and is a lumped representation of the continuous vortex sheet shed during the initial time step. As argued by Katz and Plotkin, this vortex should be placed around 0.2-0.3 of the distance covered in the time step used to discretize the wake. Once this vortex has been shed, according to Helmholtz' theorem, it follows the free-stream flow, thus under the assumption of small perturbations, the remaining wake is shed parallel to the initial free stream flow. The only parameter that is left to be investigated is the distance at which the prescribed wake is truncated. As the distance between the shedded vortices and the wing increases, their influence diminishes, allowing for a truncation of the wake after a certain distance without a major influence on the resulting aerodynamic forces and moments. The effect of this truncation will be assessed in more detail when discussing the results in section 3.

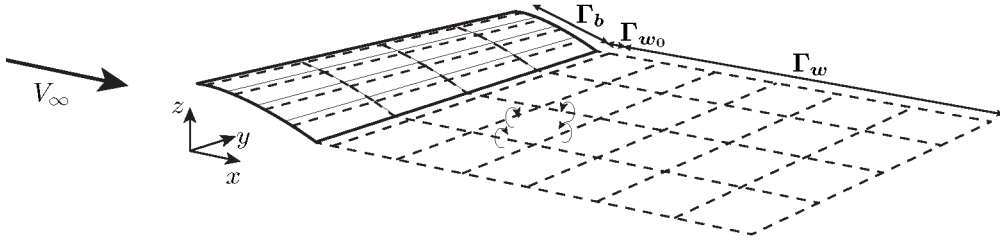


Figure 1: Example wing discretization using vortex ring elements. The thick solid lines indicate the wing outline, the thin solid lines indicate the panel distribution, and the dashed lines indicate the vortex ring elements.

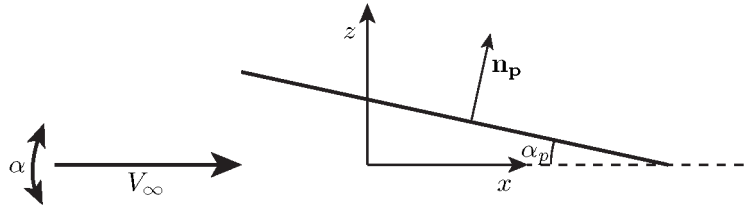


Figure 2: Schematic illustrating a panel at an angle α_p with respect to the free-stream flow.

This system of equations can now be written in a continuous-time state-space system in two steps. As a first step, the right hand side of the flow tangency condition given in equation (5) is investigated. When looking at Figure 2 illustrating a wing panel under an angle α_p with respect to the mean free stream flow, the right hand side reduces to:

$$-\mathbf{V}_\infty \cdot \mathbf{n}_p = -V_\infty \begin{pmatrix} \cos \alpha \\ \sin \alpha \end{pmatrix} \cdot \begin{pmatrix} n_{x_p} \\ n_{z_p} \end{pmatrix} = -V_\infty \begin{pmatrix} \cos \alpha \\ \sin \alpha \end{pmatrix} \cdot \begin{pmatrix} \sin \alpha_p \\ \cos \alpha_p \end{pmatrix} \quad (8)$$

where α_p is the panel angle of attack with respect to the undisturbed flow and α is the perturbation angle of the free stream flow. When small perturbations are assumed, thus making a small angle approximation for α , this reduces to:

$$-\mathbf{V}_\infty \cdot \mathbf{n}_p = -V_\infty \left(\frac{1}{\alpha} \right) \cdot \begin{pmatrix} \sin \alpha_p \\ \cos \alpha_p \end{pmatrix} = -V_\infty \sin \alpha_p - V_\infty \cos \alpha_p \cdot \alpha \quad (9)$$

Note that the first term in equation (9) is independent of the perturbation angle α , thus for this part of the flow tangency boundary condition the time dependency in the system of equations stems only from Helmholtz theorem. From a physical point of view, this can be interpreted in two ways. One, the wing is flying at a free stream velocity, V_∞ , and the wake is fully developed. In this case a solution can be found by splitting the problem in two sub-problems. First, a steady solution satisfying the first term in equation (9) is obtained assuming constant vorticity in the wake. Second, an unsteady solution satisfying the second term in equation (9) is obtained by developing the wake vorticity in time. Finally, by the principle of superposition the total aerodynamic forces and moments can be found. Two, the wing exhibits a sudden acceleration from rest to V_∞ , thus the vorticity in the wake is initially 0. In this case, the steady term in the boundary condition needs to be included in the unsteady solution and the starting vortex is also resolved.

Based on these assumptions, the unsteady aerodynamic flow problem can be written in continuous-time state-space form, similar to the derivation of Mohammadi-Amin et al.[12] for flat plates. Note that Mohammadi-Amin et al. only include the unsteady boundary condition. Starting from equation (7) for Helmholtz theorem:

$$\mathbf{H}_1 \boldsymbol{\Gamma}^t = \mathbf{H}_2 \boldsymbol{\Gamma}^{t-1} \rightarrow \boldsymbol{\Gamma}^t - \boldsymbol{\Gamma}^{t-1} = (1 - \mathbf{H}_2^{-1} \mathbf{H}_1) \boldsymbol{\Gamma}^t \quad (10)$$

this equation can be written in an equivalent continuous-time form by using a forward Euler discretisation of the transport of vorticity in the wake:

$$\dot{\boldsymbol{\Gamma}}_w^t = \frac{\boldsymbol{\Gamma}_w^t - \boldsymbol{\Gamma}_w^{t-1}}{\Delta t} = \frac{(1 - \mathbf{H}_2^{-1} \mathbf{H}_1) \boldsymbol{\Gamma}_w^t}{\Delta t} = \frac{V_\infty (1 - \mathbf{H}_2^{-1} \mathbf{H}_1) \boldsymbol{\Gamma}_w^t}{\Delta x_w} \quad (10)$$

where $\boldsymbol{\Gamma}_w$ defines the vortex strength in the wake to indicate that this equation only holds for the vortex strength of the wake panels and the time step Δt is related to the wake discretisation through the time it takes to travel the distance covered by one wake panel, Δx_w , resulting in $\frac{V_\infty \Delta t}{\Delta x_w}$. Note that all governing equations (5), (6), and (10) are now written at time t , thus allowing for a continuous time system written at time t . Dividing the vector of unknowns, $\boldsymbol{\Gamma}$, into three parts, the vortex ring strength on the body, $\boldsymbol{\Gamma}_b$, the vortex ring strength belonging to the first row of wake panels related to the Kutta condition, $\boldsymbol{\Gamma}_{w_0}$, and the remaining wake panels, $\boldsymbol{\Gamma}_w$, as also indicated in Figure 1, and using the small perturbation assumption for the flow tangency boundary condition, the governing equations can be rewritten as:

$$\mathbf{K}_1 \boldsymbol{\Gamma}_b + \mathbf{K}_2 \boldsymbol{\Gamma}_{w_0} + \mathbf{K}_3 \boldsymbol{\Gamma}_w = -V_\infty \mathbf{n}_x - V_\infty \mathbf{n}_z \cdot \boldsymbol{\alpha} \quad (11)$$

$$\mathbf{K}_4 \boldsymbol{\Gamma}_b + \mathbf{K}_5 \boldsymbol{\Gamma}_{w_0} = 0 \quad (12)$$

$$\mathbf{K}_6 \boldsymbol{\Gamma}_w + \mathbf{K}_7 \boldsymbol{\Gamma}_{w_0} = \dot{\boldsymbol{\Gamma}}_w \quad (13)$$

where \mathbf{K}_1 , \mathbf{K}_2 , and \mathbf{K}_3 are each given by a part of the aerodynamic influence coefficient matrix \mathbf{A} , \mathbf{K}_4 and \mathbf{K}_5 are matrices containing ones and zeros to link the trailing edge panel to the corresponding first wake panel as defined by equation (6), and \mathbf{K}_6 and \mathbf{K}_7 describe the transport of vorticity in the wake according to equation (10). Using equation (12), $\boldsymbol{\Gamma}_b$ can be

written as function of Γ_{w_0} . When this is inserted in equation (11), Γ_{w_0} can be written as function of Γ_w and the velocity induced by the free stream flow. Substituting this relation in the wake transport equation, the state equation of the state-space system can be derived:

$$\dot{\Gamma}_w = K_8 \Gamma_w + K_9 \alpha + K_{10} \quad (13)$$

where

$$K_8 = K_6 + K_7(K_5 - K_4 K_1^{-1} K_2)^{-1} K_4 K_1^{-1} K_3 \quad (14)$$

$$K_9 = -K_7(K_5 - K_4 K_1^{-1} K_2)^{-1} K_4 K_1^{-1} B_1 \quad (15)$$

$$K_{10} = -K_7(K_5 - K_4 K_1^{-1} K_2)^{-1} K_4 K_1^{-1} B_2 \quad (16)$$

with B_1 a diagonal matrix containing $-V_\infty n_z$ and $B_2 = -V_\infty n_x$.

Next, using the unsteady Bernoulli equation given by equation (4), the aerodynamic forces and moments can be determined. Since vortex ring elements are used, the aerodynamic forces and moments can be computed directly from the vortex strength of the vortex segments using the Kutta-Joukowski theorem, equivalent to the unsteady lifting line theory.[13] The computation of the aerodynamic forces and moments can be split in a steady component and an unsteady component. The steady component of the aerodynamic forces is given by the steady component of the Kutta-Joukowski theorem and is computed for each of the bound vortices:

$$F_{st} = \rho V_\infty \times \Gamma = \rho V_\infty \times e_r \Gamma \quad (17)$$

where e_r is the vector along the vortex segment and Γ is the vortex strength of the vortex segment. The resulting force acts at the midpoint of the bound vortex segment. Note that, in order to only account for valid aerodynamic forces (under the assumption of inviscid, irrotational flow), these forces need to be corrected by subtracting any force components that do not act in the plane spanned by the free-stream velocity and the panel normal. An example of this is given in Figure 3, where the two trailing vortices of body panel i, j are in the plane given by the free-stream velocity and the panel normal, but oriented with an angle α with respect to the free-stream flow.

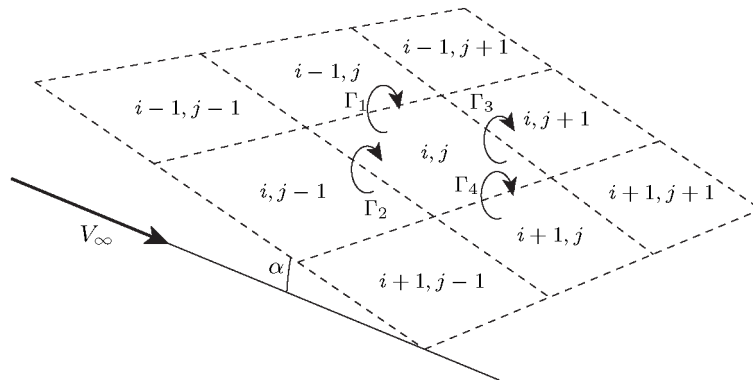


Figure 3: Schematic illustration of vortex ring element i, j and its neighbours to illustrate the computation of the aerodynamic forces.

If the forces are computed using equation (13), this results in a force component in the plane of the panel. However, since no viscous forces are accounted for, this force cannot exist and therefore should be subtracted from the forces computed by equation (13). Using Figure 3, the forces created by the 4 bound vortices that involve panel i, j are given by:

$$\mathbf{F}_{st_{i,j_1}} = \overbrace{\rho \mathbf{V}_\infty \times \mathbf{e}_{\Gamma_1} (\Gamma_{i,j} - \Gamma_{i-1,j})}^{F_1} - \frac{(\mathbf{F}_1 \cdot (\mathbf{V}_\infty \times \mathbf{n}_1)) (\mathbf{V}_\infty \times \mathbf{n}_1)}{|\mathbf{V}_\infty \times \mathbf{n}_1|^2} \quad (18)$$

$$\mathbf{F}_{st_{i,j_2}} = \overbrace{\rho \mathbf{V}_\infty \times \mathbf{e}_{\Gamma_1} (\Gamma_{i,j} - \Gamma_{i-1,j})}^{F_2} - \frac{(\mathbf{F}_2 \cdot (\mathbf{V}_\infty \times \mathbf{n}_2)) (\mathbf{V}_\infty \times \mathbf{n}_2)}{|\mathbf{V}_\infty \times \mathbf{n}_2|^2} \quad (19)$$

$$\mathbf{F}_{st_{i,j_3}} = \overbrace{\rho \mathbf{V}_\infty \times \mathbf{e}_{\Gamma_1} (\Gamma_{i,j} - \Gamma_{i-1,j})}^{F_3} - \frac{(\mathbf{F}_1 \cdot (\mathbf{V}_\infty \times \mathbf{n}_3)) (\mathbf{V}_\infty \times \mathbf{n}_3)}{|\mathbf{V}_\infty \times \mathbf{n}_3|^2} \quad (20)$$

$$\mathbf{F}_{st_{i,j_4}} = \overbrace{\rho \mathbf{V}_\infty \times \mathbf{e}_{\Gamma_1} (\Gamma_{i,j} - \Gamma_{i-1,j})}^{F_4} - \frac{(\mathbf{F}_1 \cdot (\mathbf{V}_\infty \times \mathbf{n}_4)) (\mathbf{V}_\infty \times \mathbf{n}_4)}{|\mathbf{V}_\infty \times \mathbf{n}_4|^2} \quad (21)$$

Similarly the steady component of the forces induced by the remaining bound vortices can be computed, resulting in the total aerodynamic force distribution. Note that for the bound vortices on the wing leading edge or wing tip, the vortex strength is only given by the vortex strength of that particular panel, since no neighbouring panels exist.

The unsteady component of the aerodynamic forces is given by the unsteady component of the Kutta-Joukowski theorem and is computed per panel according to:

$$\mathbf{F}_{unst_i} = \rho \hat{\mathbf{V}}_\infty \times \hat{\mathbf{e}}_{\Gamma_i} \frac{\partial \Gamma_{i,j}}{\partial t} A_{i,j} \quad (22)$$

where $\hat{\mathbf{V}}_\infty$ is the unit vector in the direction of the free stream flow velocity and $\hat{\mathbf{e}}_{\Gamma_i}$ is the unit vector in the direction of the leading vortex segment. The aerodynamic moments can be computed by defining a reference axis with respect to which the aerodynamic moments are computed.

Using equations (17) and (22) for the steady and unsteady forces, the total aerodynamic forces and moments can be related to the vortex strength according to:

$$\begin{bmatrix} \mathbf{F} \\ \mathbf{M} \end{bmatrix} = \begin{bmatrix} \mathbf{F}_{st} \\ \mathbf{M}_{st} \end{bmatrix} + \begin{bmatrix} \mathbf{F}_{unst} \\ \mathbf{M}_{unst} \end{bmatrix} = \mathbf{L}_1 \Gamma_b + \mathbf{L}_2 \dot{\Gamma}_b \quad (22)$$

Using equations (11) and (12), the vortex strength of the body panels can be related to the vortex strength of the wake panels and the input, resulting in:

$$\Gamma_b = -\mathbf{L}_3^{-1} \mathbf{K}_1^{-1} \mathbf{K}_3 \Gamma_w + \mathbf{L}_3^{-1} \mathbf{K}_1^{-1} \mathbf{B}_1 \alpha + \mathbf{L}_3^{-1} \mathbf{K}_1^{-1} \mathbf{B}_2 \quad (23)$$

where $\mathbf{L}_3 = \mathbf{I} - \mathbf{K}_1^{-1} \mathbf{K}_2 \mathbf{K}_5^{-1} \mathbf{K}_4$. Taking the time derivative of this equation, realising that all terms related to the steady component of the boundary conditions are independent of time and substituting this in equation (22), the following relation between the aerodynamic forces and moments and the vortex strength in the wake and the boundary conditions is found:

$$\begin{bmatrix} \mathbf{F} \\ \mathbf{M} \end{bmatrix} = \mathbf{L}_4 \Gamma_w + \mathbf{L}_5 \boldsymbol{\alpha} + \mathbf{L}_6 + \mathbf{L}_7 \dot{\Gamma}_w + \mathbf{L}_8 \dot{\boldsymbol{\alpha}} \quad (24)$$

where

$$\mathbf{L}_4 = -\mathbf{L}_1 \mathbf{L}_3^{-1} \mathbf{K}_1^{-1} \mathbf{K}_3 \quad (25)$$

$$\mathbf{L}_5 = \mathbf{L}_1 \mathbf{L}_3^{-1} \mathbf{K}_1^{-1} \mathbf{B}_1 \quad (26)$$

$$\mathbf{L}_6 = \mathbf{L}_1 \mathbf{L}_3^{-1} \mathbf{K}_1^{-1} \mathbf{B}_2 \quad (27)$$

$$\mathbf{L}_7 = -\mathbf{L}_2 \mathbf{L}_3^{-1} \mathbf{K}_1^{-1} \mathbf{K}_3 \quad (28)$$

$$\mathbf{L}_8 = \mathbf{L}_2 \mathbf{L}_3^{-1} \mathbf{K}_1^{-1} \mathbf{B}_1 \quad (29)$$

Finally, using equation (13), equation (24) can be reduced to:

$$\begin{bmatrix} \mathbf{F} \\ \mathbf{M} \end{bmatrix} = \mathbf{L}_9 \Gamma_w + \mathbf{L}_{10} \boldsymbol{\alpha} + \mathbf{L}_8 \dot{\boldsymbol{\alpha}} + \mathbf{L}_{11} \quad (30)$$

where $\mathbf{L}_9 = \mathbf{L}_4 + \mathbf{L}_7 \mathbf{K}_8$, $\mathbf{L}_{10} = \mathbf{L}_5 + \mathbf{L}_7 \mathbf{K}_9$, and $\mathbf{L}_{11} = \mathbf{L}_6 + \mathbf{L}_7 \mathbf{K}_{10}$. The resulting system of governing equations thus becomes:

$$\dot{\Gamma}_w = \mathbf{K}_8 \Gamma_w + \mathbf{K}_9 \boldsymbol{\alpha} + \mathbf{K}_{10} \quad (31)$$

$$\begin{bmatrix} \mathbf{F} \\ \mathbf{M} \end{bmatrix} = \mathbf{L}_9 \Gamma_w + \mathbf{L}_{10} \boldsymbol{\alpha} + \mathbf{L}_8 \dot{\boldsymbol{\alpha}} + \mathbf{L}_{11} \quad (32)$$

Therefore, identifying $[\dot{\boldsymbol{\alpha}}, 1]^T$ as state-space input, \mathbf{u} , $[\Gamma_w, \boldsymbol{\alpha}]^T$ as state vector, \mathbf{x} , and $[\mathbf{F}, \mathbf{M}]^T$ as output vector, \mathbf{y} , a standard continuous-time state-space system is obtained:

$$\dot{\mathbf{x}} = \begin{bmatrix} \mathbf{K}_8 & \mathbf{K}_9 \\ \mathbf{0} & \mathbf{0} \end{bmatrix} \mathbf{x} + \begin{bmatrix} \mathbf{0} & \mathbf{K}_{10} \\ \mathbf{I} & \mathbf{0} \end{bmatrix} \mathbf{u} \quad (33)$$

$$\mathbf{y} = [\mathbf{L}_9 \quad \mathbf{L}_{10}] \mathbf{x} + [\mathbf{L}_8 \quad \mathbf{L}_{11}] \mathbf{u} \quad (34)$$

In conclusion, under the assumption of small perturbation of a thin wing around a steady-state reference configuration, this state-space system allows for the computation of the inviscid, incompressible, irrotational, unsteady aerodynamic forces and moments of any generic wing.

3 RESULTS

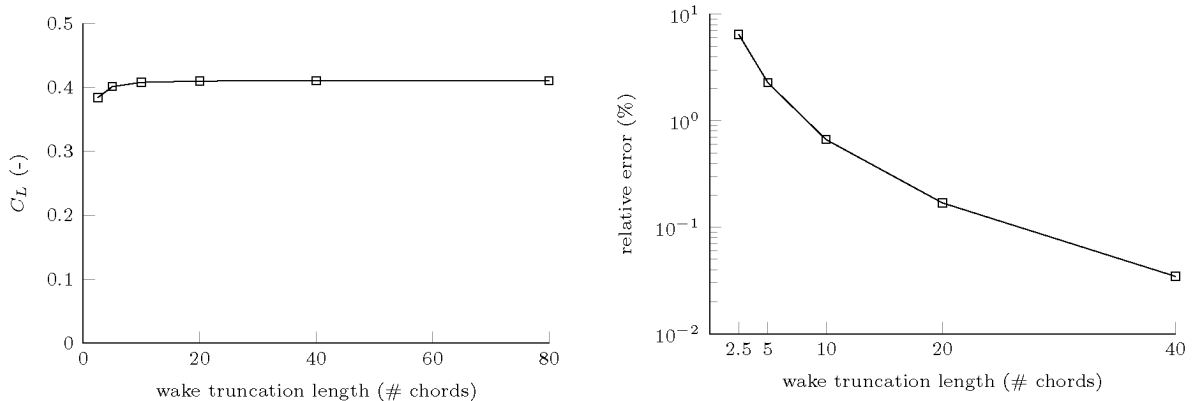
In order to assess the effect of wake truncation, first a study on the required wake length for a converged solution is carried out. Next, the state-space unsteady aerodynamic model, as described in section 2, is assessed by first running the model for different steady and unsteady test cases, followed by a pitch-plunge analysis study to indicate the advantages of the current model to existing models. For all results presented, first a mesh convergence study has been carried out, but for clarity, only the results for a converged mesh will be shown. In case of the unsteady aerodynamic results, a study on the required wake length in terms of the number of chords is first carried out in order to assess the effect of wake truncation on the unsteady aerodynamic results, before the results of the model are compared to the literature.

3.1 Wake truncation

The effect of wake truncation on the aerodynamic loads is investigated by analysing a rectangular wing with an aspect ratio of 8, and properties given in Table 1. The wing is suddenly accelerated from rest and the effect of wake truncation is assessed by investigating the lift coefficient after the wing has travelled a distance of 100 chord lengths. The selected flight speed is 10 m/s at sea level. The resulting lift coefficient for different wake truncation lengths is given in Figure 4a. In order to do a more thorough assessment of the actual error, the relative error of the lift coefficient at different wake truncation lengths with respect to the longest wake truncation length of 80 chords is shown in Figure 4b. As can be seen, depending on the level of accuracy required, a wake length of 20 or 40 chords is sufficient for a converged solution to within 0.2% or 0.05% respectively. Note that, even though this provides an indication of the effect of wake truncation, the effect of the wake truncation length might be different for each wing and flight condition analysed and should therefore always be considered as a parameter in a convergence study of the results.

Semispan	0.40 m
Chord	0.10 m
Sweep angle	0 deg
Camber	0%

Table 1: Wing properties



(a) Convergence study showing the lift coefficient for various lengths of wake truncation.

(b) Convergence study showing the relative error for various lengths of wake truncation with respect to a wake length of 80.

Figure 4: Effect of wake truncation on the lift coefficient of a rectangular wing with an aspect ratio of 8, suddenly accelerating from rest after it has travelled 100 chords.

3.2 Verification

In order to verify the unsteady aerodynamic model, the model is applied to several benchmark problems. First, a steady verification of the model is done by comparing the results of the current approach to steady aerodynamic results in the literature, as shown in section 3.2.1. Then in section 3.2.2, the verification is completed by comparing the model to unsteady aerodynamic results in the literature.

3.2.1 Steady aerodynamic verification

Aircraft wings in general are not rectangular, but have a combination of taper, sweep, dihedral, twist, and camber for optimal aerodynamic performance. Therefore, as a steady verification, the results obtained by the current model are compared to results found in literature for different taper ratios, sweep angles, dihedral, twist angles, and camber. For all cases presented in this section, the wing has been discretised using 16 spanwise and 32 chordwise elements. First, as a verification of the implementation of camber, a wing with an aspect ratio of 200 is modelled to approximate 2D aerodynamics with different levels of camber and compared to results obtained by Xfoil.[14] In order to do a fair comparison to the 2D results, the results obtained from Xfoil have been compared to the section lift coefficient at the center of the wing. The results of this comparison are shown in Figure 5, showing excellent agreements in the linear aerodynamic range. As can be seen, as the angle of attack increases above 8 deg or decreases below -6 deg the results start to differ because of nonlinear aerodynamic effects captured by Xfoil, which cannot be captured using thin airfoil theory. As can be seen, as the level of camber increases, these nonlinear effects become more pronounced and thus the difference between the present model and Xfoil increases. However, most aircraft don't have these highly cambered airfoils and fly at small angles of attack, where the present model provides excellent results.

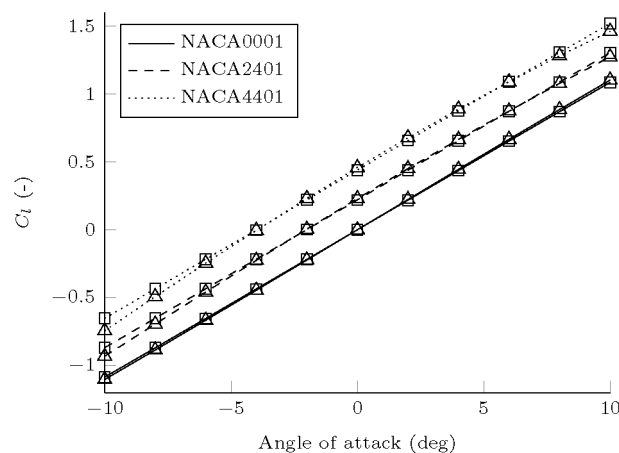
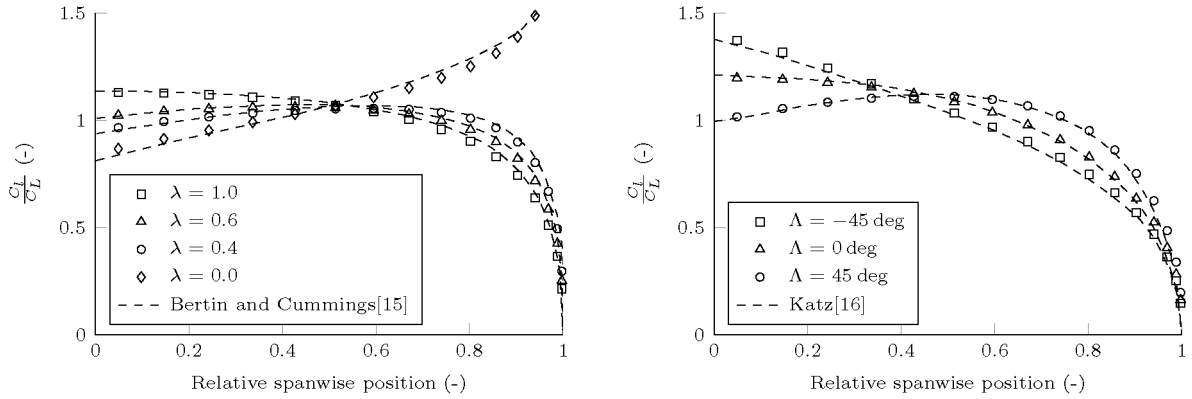


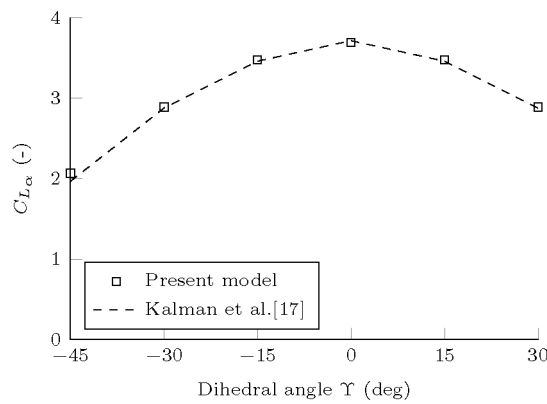
Figure 5: Verification of the steady aerodynamic results for a 2D cambered airfoil. The squares indicate the present model and the triangles indicate the data obtained from Xfoil.

Second, Figure 6a shows the comparison of the current model to the results obtained by Bertin and Cummings[15] using lifting-line theory for an untwisted wing with an aspect ratio of 7.28 and a NACA2412 airfoil at various taper ratios. As can be seen, the results show good agreement for a taper ratio of 0.4, 0.6, and 1.0. Only for a taper ratio of 0, the difference becomes more pronounced. Note that using vortex rings, a taper ratio of 0 can only be approximated by selecting a very small taper ratio of, in this case, 0.001, since otherwise the length of vortices at the wing tip would become zero, resulting in numerical problems when solving the system of equations. Furthermore, the difference can be explained by the fact that both models use a different approximation of the lift distribution; Bertin and Cummings use lifting-line theory with a truncated series to approximate the lift distribution, while in the present model the wing is discretised in spanwise and chordwise direction. Noting that general aircraft do not have a taper ratio of 0, this should not provide any difficulties in analysing general aircraft wings.



(a) An untwisted wing with a NACA2412 airfoil and an aspect ratio of 7.28 at different taper ratios.

(b) An untwisted wing with an aspect ratio of 4 at different sweep angles.



(c) An untwisted wing with an aspect ratio of 4 at different dihedral angles.

Figure 6: Verification of 3D steady aerodynamics results.

Third, Figure 6b shows the comparison for an untwisted, untapered wing with an aspect ratio of 4.0 at different sweep angles to the results obtained by Katz.[16] Since Katz' model is based on the unsteady vortex lattice method, and is thus equivalent to the current model, as expected, the results show excellent agreement.

Finally, in order to verify the model for dihedral, the results of the model were compared to the results by Kalman et al.[17] for a rectangular wing with an aspect ratio of 4.0 at different dihedral. As can be seen in Figure 6c, the results show excellent agreement.

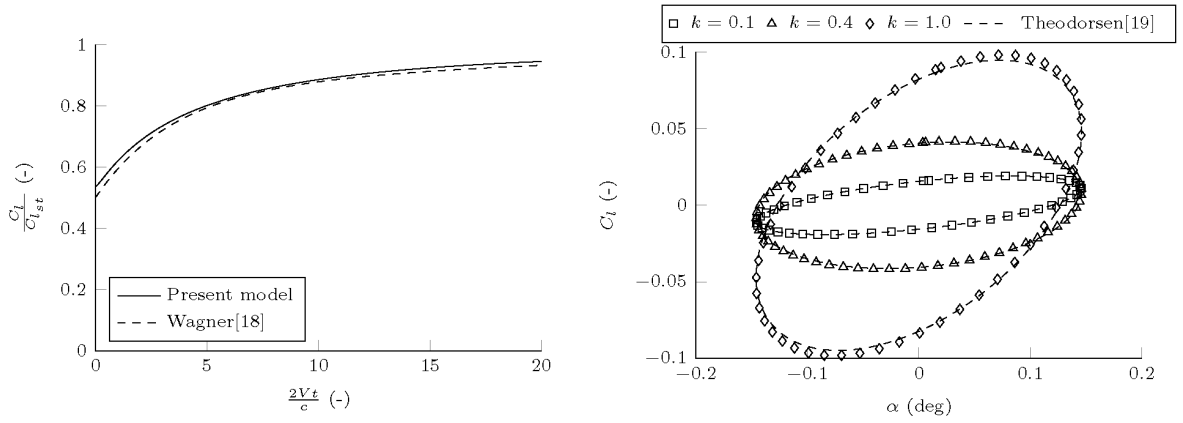
In conclusion, the steady results show excellent agreement to results found in the literature for different taper ratios, sweep angles, dihedral, and twist, thus verifying the current aerodynamic model for steady aerodynamic analysis.

3.2.2 Unsteady aerodynamic verification

In order to verify the unsteady aerodynamic response, similar to the steady aerodynamic results, the unsteady aerodynamic model is first compared to 2D unsteady results in the literature. Figure 7a shows the comparison of the present model to the analytical approximation of Wagner[18] for a 2D flat plate under a sudden acceleration, which is equivalent to a step response of the angle of attack or the impulse response of the current

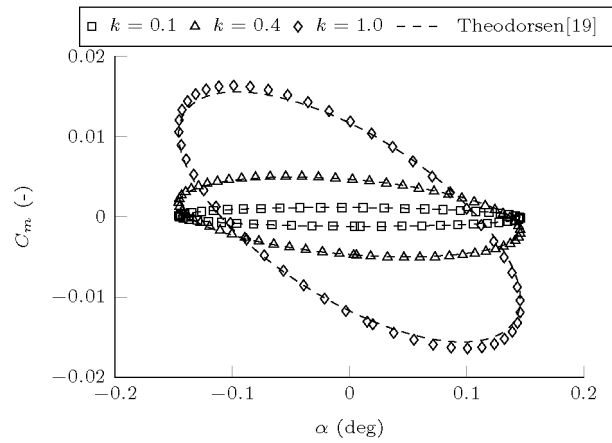
system. The wing is discretised using 8 spanwise and 32 chordwise elements. The wake is truncated at 10 times the chord and the normalised time step is given by $\frac{V_\infty \Delta t}{c} = \frac{1}{32}$. As can be seen, the initial lift is slightly over predicted by the present model, after which the model converges to the solution of Wagner and shows excellent agreement. This initial over prediction of the lift can be explained by the fact that the present model, due to its wake discretisation, can only represent a finite acceleration rate and not the infinite acceleration rate as solved by Wagner. As was shown by Katz[16], the effect of this finite acceleration rate is to moderately increase the lift.

Figure 7b and Figure 7c show the comparison of the present model to the lift and moment coefficient as predicted by Theodorsen[19] for the harmonic pitch, plunge oscillation of a 2D flat plate at different reduced frequencies. The flat plate pitches around the quarter-chord axis with an amplitude of 1 deg and has a plunge amplitude of $\frac{h_0}{b} = 0.2$, $\frac{h_0}{b} = 0.05$, and $\frac{h_0}{b} = 0.02$ for $k = 0.1$, $k = 0.4$, and $k = 1$ respectively. The wing is discretised using 8 spanwise and 32 chordwise elements. The wake is truncated at 20 times the chord and the normalised time step is given by $\frac{V_\infty \Delta t}{c} = \frac{1}{32}$. As can be seen the present model shows excellent agreement for $k = 0.1$ and $k = 0.4$. At $k = 1$, it can be seen that the present model slightly overpredicts the lift and moment coefficient, which can be explained by the fact that for the present model the wake needs to be discretised, while Theodorsen computes the lift and moment coefficient analytically. Especially at higher reduced frequencies, the effect of this discretisation becomes more pronounced, since the number of wake panels travelled per oscillation becomes smaller. It should be noted, however, that, for most practical applications, a reduced frequency of 0.4 is already very high.



(a) Sudden acceleration of a 2D flat plate.

(b) Harmonic pitch, plunge oscillation of a 2D flat plate at different reduced frequencies.



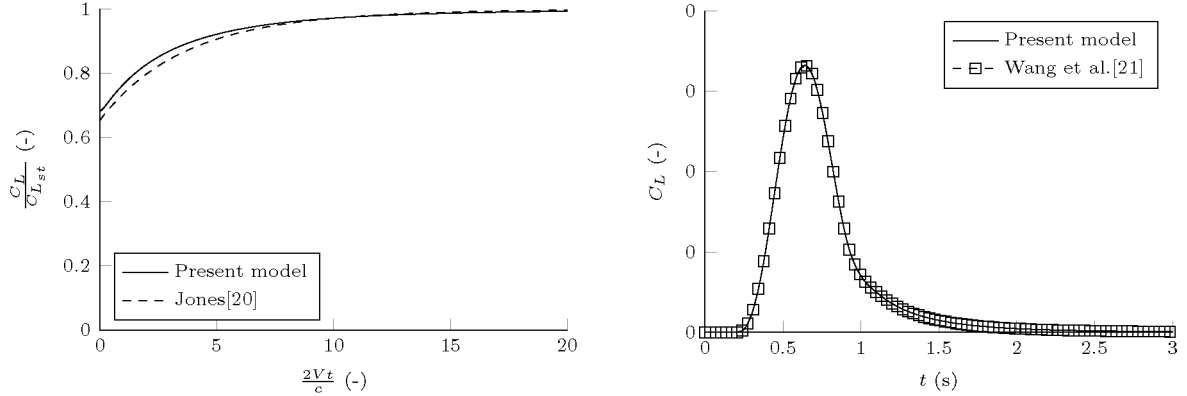
(c) Harmonic pitch, plunge oscillation of a 2D flat plate at different reduced frequencies.

Figure 7: Verification of 2D unsteady aerodynamics results.

Aircraft in general have a combination of taper, sweep, dihedral, twist, and camber. However, to the authors knowledge, no results are available in literature on the unsteady aerodynamic response of panel methods for thin general aircraft wings. Therefore, in order to verify the 3D unsteady aerodynamic response, the present model is compared to the unsteady aerodynamic response for rectangular wings. Figure 8a shows the comparison of the present model to the sudden acceleration of a flat rectangular wing with an aspect ratio of 6 to the results obtained by Jones[20]. The wing is discretised using 8 spanwise and 32 chordwise elements. The wake is truncated at 10 times the chord and the normalised time step is given by $\frac{V_\infty \Delta t}{c} = \frac{1}{32}$. As can be seen, similar to the sudden acceleration of a 2D flat plate, the present model initially overpredicts the lift because of the finite acceleration rate, before it converges to the results obtained by Jones.

As a final verification for the unsteady aerodynamic response, the present model is compared to the results obtained by Wang et al.[21] for the gust response of the Golland wing under a 1-cosine gust. The wing is discretised using 8 spanwise and 32 chordwise elements. The wake is truncated at 10 times the chord and the normalised time step is given by $\frac{V_\infty \Delta t}{c} = \frac{1}{32}$. As can be seen in Figure 8b, the results show excellent agreement, thus verifying the present model. In

conclusion, the present model shows excellent agreement to results in the literature for the unsteady aerodynamic response of wings, thus verifying the present model.



(a) Sudden acceleration of a rectangular wing with an aspect ratio of 6. (b) Gust response of the Golland wing under a 1-cosine gust.

Figure 8: Verification of 3D unsteady aerodynamics results.

3.2.3 Pitching-plunging wing

Finally, to illustrate the advantages of the present continuous-time state-space model over discrete-time models, the model is applied to the analysis of a rectangular wing with the properties given in Table 2 under a pitch, plunge motion.

Semispan	4.0 m
Chord	1.0 m
Sweep angle	0 deg
Camber	0%

Table 2: Wing properties

The free-stream velocity is set to 50 m/s at sea level and the wing is perturbed at reduced frequencies of $k = 0.1$, $k = 0.4$, and $k = 1$, using the following input signal:

$$\theta(t) = \theta_0 \sin\left(\frac{kV_\infty t}{b}\right) \quad (35)$$

$$h(t) = h_0 \cos\left(\frac{kV_\infty t}{b}\right) \quad (36)$$

where θ is the pitch angle, θ_0 is the pitch amplitude, h is the plunge displacement, and h_0 is the plunge amplitude. The wing pitches about the quarter chord with an amplitude of 1 deg and plunges with an amplitude of $\frac{h_0}{b} = 0.2$, $\frac{h_0}{b} = 0.05$, and $\frac{h_0}{b} = 0.02$ for $k = 0.1$, $k = 0.4$, and $k = 1$ respectively. The number of spanwise vortex ring elements is kept constant at 8, while the number of chordwise panels and correspondingly the wake discretisation is varied. All results presented are obtained for a fully developed wake.

The resulting convergence study is shown in Figure 9a. Since no analytical or reference solution is available for this case, the relative error of the maximum lift coefficient with

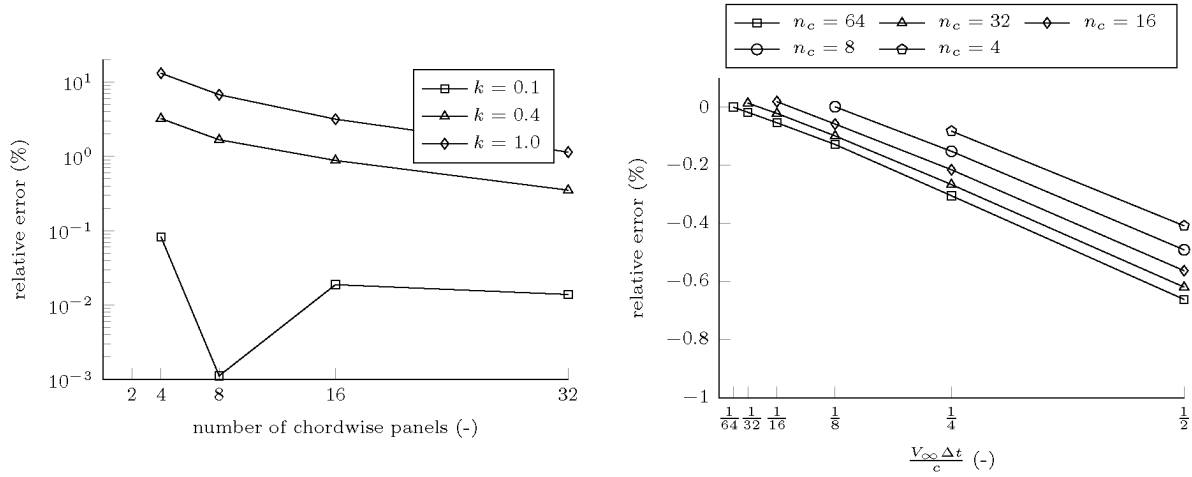
respect to the result obtained with the finest mesh is plotted. The resulting maximum lift coefficient found for the finest mesh is given in Table 3.

Red. frequency	Lift coefficient
0.1	0.188
0.4	0.155
1.0	0.192

Table 2: Lift coefficient for different reduced frequencies

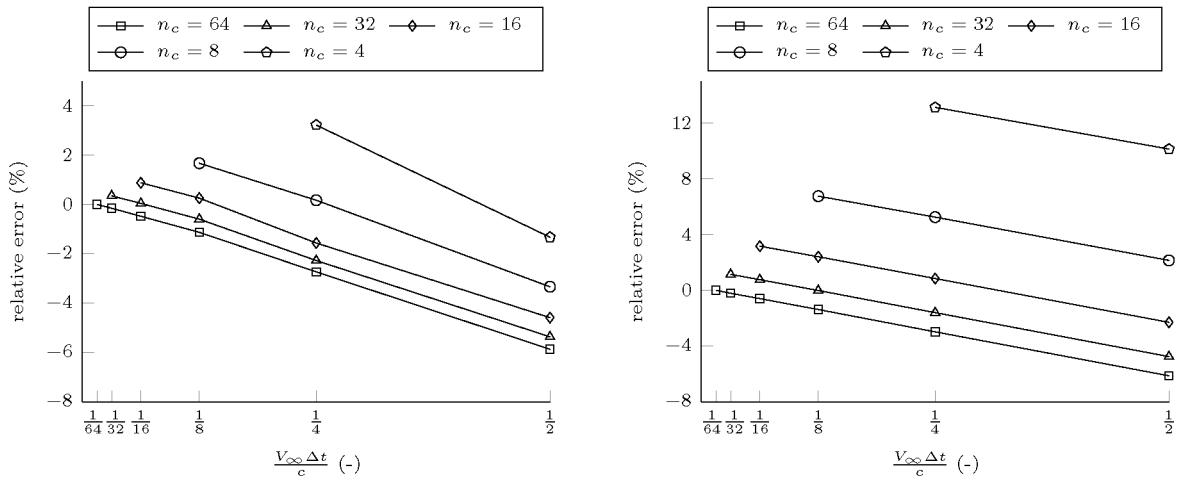
As is expected, as the reduced frequency increases, a finer wake discretisation is required to obtain a converged solution, since the number of wake panels travelled per oscillation decreases. For $k = 0.1$, 4 chordwise panels is already sufficient to find a solution within 0.1% of the solution found for 64 chordwise panels, while for $k = 0.4$, in order to bring the error with respect to the solution for $n_c = 64$ to 1%, already 16 chordwise panels are required, and for $k = 1$, 64 chordwise panels are required.

When looking at Figure 9, another interesting observation can be made when looking at the convergence trend for $k = 0.1$. While $k = 0.4$, and $k = 1$ converge monotonically from above, as can also be concluded from Figure 9c and Figure 9d, for $k = 0.1$ the maximum lift coefficient first increases up to 16 chordwise panels after which it also converges from above. This can be explained by a combination of two sources of error. The first source of error comes from the spatial discretization of the wing for which the lift coefficient will converge from above. The second source of error comes from the time discretization of the solution, where, as the mesh is refined and thus the time discretization is refined, the time discretization converges to the time at which the maximum lift occurs, for which the lift coefficient converges from below. In case of $k = 0.4$ and $k = 1$, the spatial discretization introduces an error that is much larger than the error introduced by the time discretization, thus resulting in a solution which converges from above. However, in case of $k = 0.1$, initially the error introduced by the time discretization is larger than the error introduced by the spatial discretization, resulting in an increasing lift coefficient, while as the mesh and thus time discretization is refined, the error introduced by the spatial discretization becomes more important, resulting in convergence from above.



(a) Convergence study showing the relative error of various mesh size with respect to the analyses for $n_c = 64$.

(b) Effect of varying the timestep for time integration on the lift coefficient for various mesh sizes at a reduced frequency of $k = 0.1$.



(c) Effect of varying the timestep for time integration on the lift coefficient for various mesh sizes at a reduced frequency of $k = 0.4$.

(d) Effect of varying the timestep for time integration on the lift coefficient for various mesh sizes at a reduced frequency of $k = 1.0$.

Figure 9: Pitch, plunge analysis of a rectangular wing with an aspect ratio of 8.

In case of the use of a discrete-time system for general aircraft, where many different load cases and gust analysis need to be run, either many different models are required for efficient analyses for each of the cases or a single model refined enough for the most demanding load case, but inefficient for the other load cases, is required. However, in case of the continuous-time state-space model, another trade-off can be made, where a single fine model is used for the model setup, but the efficiency of the analysis is increased by increasing the time step when permitted. Especially in combination with a reduced-order modelling technique, this results in a single model that is both accurate and efficient. Figure 9b, Figure 9c, and Figure 9d show this trade-off for the different reduced frequencies. As can be seen, for, for example $k = 0.1$, a normalised time-step of $1/2$ is already sufficient for a maximum lift coefficient within 1% of the solution found for a timestep of $1/64$. This results in a decrease in computational time of the time integration by a factor of 32, which reduces total

computational time significantly, especially when many simulations need to be run. Note that, even for $k = 1$, the timestep can be increased by a factor of 2, while keeping the error to within 1%, thus clearly showing the advantage of a variable time step.

4 CONCLUSIONS

A continuous-time state-space unsteady aerodynamic model has been presented for efficient load analysis of general aircraft wings. Based on potential flow theory, under a thin wing assumption, the unsteady vortex lattice method is used to setup the governing discretised equations. By assuming small perturbances with respect to the steady solution, the flow tangency condition can be linearised. Finally, by assuming a fixed wake, the governing continuous-time state-space system has been derived. The states of the system are the vortex strength of the wake vortex elements and the perturbation angle of attack, and the input of the system is the time derivative of the perturbation angle of attack. Verification of the present approach with results in the literature, both for steady and unsteady aerodynamic solutions, and 2D and 3D solutions for general wing shapes, shows excellent agreement. Finally, the present model has been applied to the pitch-plunge analysis of a rectangular wing with an aspect ratio of 8, showing the benefits of the present approach over discrete-time models, by allowing for a single model to be applied to all load cases, while varying the time step for efficiency.

In conclusion, the resulting model can be used for the efficient loads analysis of general aircraft wings, and its state-space implementation allows for easy integration with structural or flight dynamic models, allowing for efficient aero(servo)elastic analysis using a time step solely governed by accuracy requirements.

5 REFERENCES

- [1] J. Murua, R. Palacios, and J. M. R. Graham, “Applications of the unsteady vortex-lattice method in aircraft aeroelasticity and flight dynamics,” *Progress in Aerospace Sciences*, vol. 55, pp. 46–72, Nov. 2012.
- [2] T. Kier, “Comparison of Unsteady Aerodynamic Modelling Methodologies with Respect to Flight Loads Analysis,” in *AIAA Atmospheric Flight Mechanics Conference and Exhibit*, American Institute of Aeronautics and Astronautics.
- [3] M. J. Patil, D. H. Hodges, and C. E. S. Cesnik, “Nonlinear Aeroelasticity and Flight Dynamics of High-Altitude Long-Endurance Aircraft,” *Journal of Aircraft*, vol. 38, no. 1, pp. 88–94, 2001.
- [4] M. J. Patil and D. H. Hodges, “On the importance of aerodynamic and structural geometrical nonlinearities in aeroelastic behavior of high-aspect-ratio wings,” *Journal of Fluids and Structures*, vol. 19, no. 7, pp. 905–915, Aug. 2004.
- [5] D. A. Peters, S. Karunamoorthy, and W.-M. Cao, “Finite state induced flow models. I - Two-dimensional thin airfoil,” *Journal of Aircraft*, vol. 32, no. 2, pp. 313–322, 1995.
- [6] J. G. Leishman and K. Q. Nguyen, “State-space representation of unsteady airfoil behavior,” *AIAA Journal*, vol. 28, no. 5, pp. 836–844, May 1990.
- [7] E. ALBANO and W. P. RODDEN, “A doublet-lattice method for calculating lift distributions on oscillating surfaces in subsonic flows.,” *AIAA Journal*, vol. 7, no. 2, pp. 279–285, 1969.
- [8] K. Roger, “Airplane math modelling and active aeroelastic control design,” AGARD-CP-228, 1977.

- [9] M. Karpel, “Design for Active Flutter Suppression and Gust Alleviation Using State-Space Aeroelastic Modeling,” *Journal of Aircraft*, vol. 19, no. 3, pp. 221–227, 1982.
- [10] J. Katz and A. Plotkin, *Low-Speed Aerodynamics*. Cambridge: Cambridge University Press, 2001.
- [11] K. C. Hall, “Eigenanalysis of unsteady flows about airfoils, cascades, and wings,” *AIAA Journal*, vol. 32, no. 12, pp. 2426–2432, 1994.
- [12] M. Mohammadi-Amin, B. Ghadiri, M. M. Abdalla, H. Haddadpour, and R. De Breuker, “Continuous-time state-space unsteady aerodynamic modeling based on boundary element method,” *Engineering Analysis with Boundary Elements*, vol. 36, no. 5, pp. 789–798, 2012.
- [13] M. Drela, “Integrated simulation model for preliminary aerodynamic, structural, and control-law design of aircraft,” in *40th Structures, Structural Dynamics, and Materials Conference and Exhibit*, American Institute of Aeronautics and Astronautics, 1999.
- [14] M. Drela, “XFOIL: An Analysis and Design System for Low Reynolds Number Airfoils,” in *Low Reynolds Number Aerodynamics*, T. J. Mueller, Ed. Springer Berlin Heidelberg, 1989, pp. 1–12.
- [15] J. J. Bertin and R. M. Cummings, *Aerodynamics for Engineers*. Pearson Education, Inc., 2009.
- [16] J. Katz, “Calculation of the Aerodynamic Forces on Automotive Lifting Surfaces,” *J. Fluids Eng.*, vol. 107, no. 4, pp. 438–443, Dec. 1985.
- [17] T. P. KALMAN, W. P. RODDEN, and J. P. GIESING, “Application of the Doublet-Lattice Method to Nonplanar Configurations in Subsonic Flow,” *Journal of Aircraft*, vol. 8, no. 6, pp. 406–413, 1971.
- [18] H. Wagner, “Über die Entstehung des dynamischen Auftriebes von Tragflügeln,” *Z. angew. Math. Mech.*, vol. 5, no. 1, pp. 17–35, Jan. 1925.
- [19] T. Theodorsen, “General Theory of Aerodynamic Instability and the Mechanism of Flutter,” NACA, 1935.
- [20] W. P. Jones, “Aerodynamic Forces on Wings in Non-uniform Motion,” H.M. Stationery Office, ARC-2117, 1945.
- [21] Z. Wang, P. C. Chen, D. D. Liu, and D. T. Mook, “Nonlinear-Aerodynamics/Nonlinear-Structure Interaction Methodology for a High-Altitude Long-Endurance Wing,” *Journal of Aircraft*, vol. 47, no. 2, pp. 556–566, 2010.

COPYRIGHT STATEMENT

The authors confirm that they, and/or their company or organization, hold copyright on all of the original material included in this paper. The authors also confirm that they have obtained permission, from the copyright holder of any third party material included in this paper, to publish it as part of their paper. The authors confirm that they give permission, or have obtained permission from the copyright holder of this paper, for the publication and distribution of this paper as part of the IFASD 2015 proceedings or as individual off-prints from the proceedings.